

Quantitative and Isolated Measurement of Far-Field Light Scattering by a Single Nanostructure

Donghyeong Kim,¹ Kwang-Yong Jeong,² Jinhyung Kim,¹ Ho-Seok Ee,¹ Ju-Hyung Kang,²
Hong-Gyu Park,² and Min-Kyo Seo^{1,*}

¹*Department of Physics and Institute for the NanoCentury, KAIST, Daejeon 34141, Republic of Korea*

²*Department of Physics, Korea University, Seoul 02841, Republic of Korea*

(Received 24 April 2017; revised manuscript received 9 September 2017; published 10 November 2017)

Light scattering by nanostructures has facilitated research on various optical phenomena and applications by interfacing the near fields and free-propagating radiation. However, direct quantitative measurement of far-field scattering by a single nanostructure on the wavelength scale or less is highly challenging. Conventional back-focal-plane imaging covers only a limited solid angle determined by the numerical aperture of the objectives and suffers from optical aberration and distortion. Here, we present a quantitative measurement of the differential far-field scattering cross section of a single nanostructure over the full hemisphere. In goniometer-based far-field scanning with a high signal-to-noise ratio of approximately 27.4 dB, weak scattering signals are efficiently isolated and detected under total-internal-reflection illumination. Systematic measurements reveal that the total and differential scattering cross sections of a Au nanorod are determined by the plasmonic Fabry-Perot resonances and the phase-matching conditions to the free-propagating radiation, respectively. We believe that our angle-resolved far-field measurement scheme provides a way to investigate and evaluate the physical properties and performance of nano-optical materials and phenomena.

DOI: [10.1103/PhysRevApplied.8.054024](https://doi.org/10.1103/PhysRevApplied.8.054024)

I. INTRODUCTION

Far-field scattering of light plays a key role in understanding the interaction between near-field effects and free-propagating radiation in optical nanostructures [1]. Considerable effort has been made in recent years to engineer optical nanostructures and investigate their physical properties of light scattering to facilitate a variety of applications including optical sensing [2,3], metamaterials and metasurfaces [4–6], holography [7], optical nonlinearity enhancement [8–11], and optomechanical systems [12,13]. The most important physical parameters for characterizing the far-field scattering properties of an optical nanostructure are the extinction cross section and the total and differential scattering cross sections, which can be efficiently enhanced using the optical resonances of the nanostructure [14,15]. To obtain the full benefits of nano-optical light scattering and realize desirable applications, it is necessary to measure and manipulate the differential scattering cross section [16,17]. While the quantitative measurements of the extinction and absorption cross sections have been reported [18,19], the total scattering cross section for a single nanostructure has been measured only indirectly using the dipole approximation [20] or estimated evaluating an array or colloid of nanostructures [21].

Fourier imaging using the back focal plane of an objective lens or parabolic mirror has typically been used to measure the far-field properties of optical nanostructures [22–25]. However, conventional back-focal-plane imaging can cover only a limited solid angle corresponding to the numerical aperture (NA) of the objective lens or parabolic mirror. Unavoidable optical aberration and distortion also require appropriate corrections by a complicated series of optical components [26]. On the other hand, direct solid-angle scanning based on a goniometer, commonly used in the radio- and microwave-frequency regimes [27], can cover the full hemispherical region or an even wider region and can also be applied to the optical-frequency regime [28–30]. In addition, direct solid-angle scanning is expected to enable quantitative far-field measurement with only a simple responsivity calibration of the employed photoreceiver, whereas most studies to date have measured the far-field radiation of single optical nanostructures in arbitrary units [16,31].

In this work, we quantitatively measure the differential far-field scattering cross-section distribution of a single Au nanorod over the full hemisphere using a solid-angle scanning system. Careful calibration of the photoreceiver enables a high signal-to-noise ratio of approximately 27.4 dB in measurement of the scattering cross section. In contrast to the emitted light, e.g., luminescence or thermal radiation, the elastic scattering radiation is difficult to distinguish from the rest of the incident light, which is not coupled to the nanostructure, using spectral filters or polarizers. To naturally isolate the scattering signal,

*Corresponding author.
minkyseo@kaist.ac.kr

we employ total-internal-reflection (TIR) illumination. Systematic measurements experimentally reveal that the total and differential far-field scattering cross sections of the Au nanorod depend on different mechanisms, the Fabry-Perot (FP) resonances of surface-plasmon polaritons (SPPs), and the phase-matching conditions to the free-propagating radiation, respectively. All the experimental results are excellently reproduced by finite-difference time-domain (FDTD) simulation and the dipole radiation interference model.

II. DIRECT SOLID-ANGLE SCANNING AND ISOLATION OF FAR-FIELD LIGHT SCATTERING

The far-field scattering distribution of the single Au nanorod is measured using a homebuilt solid-angle scanning system, as shown in Fig. 1. To cover the full hemisphere, the sample stage rotates from 0° to 180° in the azimuthal (ϕ) direction, and the detection unit rotates from -90° to $+90^\circ$ in the polar (θ) direction. The detection unit measures the far-field radiation in the Fraunhofer region 20 cm from the sample. The angular resolution of approximately 1.17° is determined by the aperture diameter of the iris (4.1 mm) in front of the collecting lens. To isolate the weak scattering signal of a single optical nanostructure from the background, we employ TIR illumination [Figs. 1(a) and 2(a)]. Under TIR illumination, part of the incident light interacts with the nanostructure and gains additional momentum that enables it to escape from the glass-air interface in the form of scattered light. The rest of the incident light uncoupled to the nanostructure is bound at the interface as an evanescent wave and eventually reflects back to the substrate. Thus, the far-field scattering

distribution and cross section of a single nanostructure can be isolatedly measured.

Figures 2(b) and 2(c) show the results of FDTD simulations using the total-field scattered-field method, which reveal that the radiation profiles in air in the total- and scattered-field regions are indeed identical. Au nanorods are highly useful for examining the far-field scattering properties because of their simple geometry and plasmonic behaviors [33–35]. SPPs propagating along the Au nanorod contribute to the spatial interference and resonant behavior of the far-field scattering distribution. In the simulations, we employ the Drude critical point model to fit the experimental dielectric function of Au [36] and set the refractive index of glass to 1.515.

Au nanorods are fabricated on a glass cover slip by typical electron-beam lithography (EBL) using a poly (methylmethacrylate) (PMMA) layer. To avoid charging of the glass substrate during the EBL process, an additional layer of a conductive polymer (Espacer 300Z, Showa Denko) is coated on the PMMA layer. The EBL pattern is developed by immersion in a 1:3 methyl isobutyl ketone: isopropyl alcohol solution at room temperature. A 1-nm-thick Cr adhesion layer and 50-nm-thick Au layer are then deposited by electron-beam evaporation, and a lift-off process with acetone finally yields the Au nanorods. The width and thickness of the nanorods are fixed at 80 and 50 nm, respectively, and the length varies from 300 to 600 nm [Figs. 2(d) and 4(c)].

Figure 2(e) shows a dark-field optical microscope image of the fabricated Au nanorod and a two-dimensional grating. The two-dimensional grating of Au nanodisks [Fig. 2(f)] is used to identify and align the TIR incident light spot under the TIR condition. The incident light weakly focused by an aspheric lens ($10\times$, $NA = 0.25$) illuminates an ellipselike

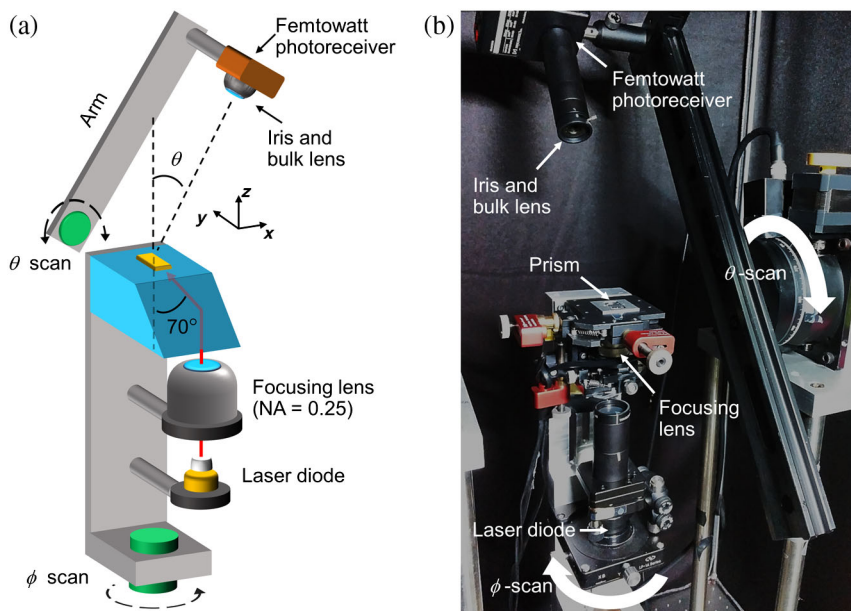


FIG. 1 (a) Schematic and (b) photo of the direct solid-angle scanning far-field measurement system. The detection unit consists of a femtowatt photoreceiver, bulk lens, and iris diaphragm [32]. The direct scanning method does not suffer from any optical distortion or aberration, so a careful calibration of the detection unit for the 660-nm laser enables quantitative measurement of the differential far-field scattering cross section as it is. The target nanostructure fabricated on the glass substrate is located on the trapezoidal prism supporting TIR illumination with an incident angle of 70° .

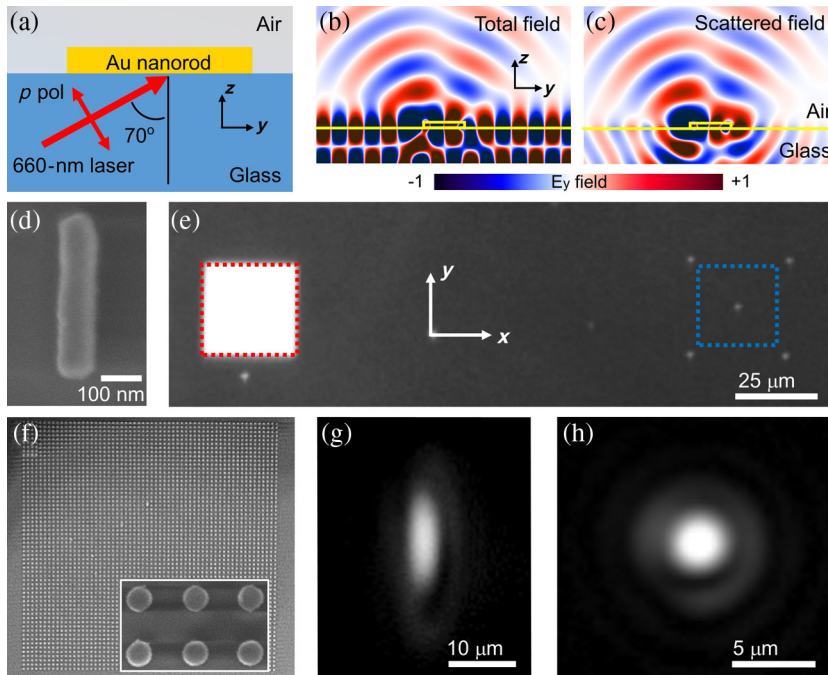


FIG. 2 Isolation of light scattering by a single Au nanorod. (a) Schematic showing the employed TIR illumination. (b),(c) Simulated total and scattered fields of the light scattering by a single 600-nm-long Au nanorod. (d) SEM image of the fabricated Au nanorod. (e) Dark-field optical microscope image of the two-dimensional grating (bright area in the red dotted box) and a single Au nanorod (bright single spot in the blue dotted box). (f) SEM image of the grating for identifying the TIR incident beam spot. The square-lattice grating consists of 200-nm-diameter Au nanodisks with a 475-nm period (inset). (g) Optical microscope image of the TIR illumination spot scattered by the grating. (h) Optical microscope image of isolated scattering by a single Au nanorod. The NA of the objective of the add-on microscope is 0.10.

area of approximately $10 \times 3 \mu\text{m}^2$ [Fig. 2(g)]. The oblique TIR illumination causes the ellipselike spot, the major axis of which is on the y axis parallel to the incidence plane. When the single Au nanorod is located at the center of the incident light spot, bright scattering is observed, as shown in the optical microscope image in Fig. 2(h). The efficient suppression of the uncoupled incident light enables the observation of this bright, isolated scattering signal with a high signal-to-background ratio. However, the optical microscope image in the Fresnel region shows only an Airy-function-like scattering pattern resulting from the NA of the objective lens and the scale of the nanorod, which is on the order of the wavelength or less. The Airy-function-like pattern indicates that the objective lens acts as a low-pass filter in the spatial frequency domain and collects only part of the information on the far-field scattering. The images in Figs. 2(g) and 2(h) are obtained by an optical microscope added to the far-field measurement setup [32].

III. QUANTITATIVE MEASUREMENTS OF FAR-FIELD SCATTERING DISTRIBUTION AND CROSS SECTION

To quantify the angular density of the scattering intensity on the hemisphere, we calibrate the responsivity of the detection unit to the 660-nm laser [32] and measure the power of the radiation scattered through the solid angle of the iris aperture area (approximately 3.30×10^{-4} sr). The incident power density of the laser is obtained by determining the effective area of TIR illumination from the optical microscope image in Fig. 2(g) [32]. Finally, the differential scattering cross section, that is, the intrinsic detection rate of the scattered photons at a given angle (θ, ϕ) , is defined as

the angular density of the scattering intensity divided by the incident power density of the laser. The profile of the measured far-field scattering distribution is projected onto a two-dimensional space using a mapping $(x, y) = (\theta \cos \phi, \theta \sin \phi)$ [Fig. 3(a)].

Figure 3(b) shows the measured differential far-field scattering cross-section distributions of Au nanorods with different lengths. The Au nanorod generates multiple scattering radiation lobes to the far field along the meridian in the y - z plane parallel to its axis. As the length of the nanorod increases, the scattering radiation lobes continuously move in the $-y$ direction, and new lobes with higher orders emerge successively from the $+y$ direction. The lobes become weaker and eventually disappear as they reach the horizon due to the substrate effect. The oblique TIR illumination causes the asymmetric distribution and movement of the far-field scattering radiation. The number and direction of scattering lobes are determined by the phase-matching condition, which depends on both the length of the nanorod and the wavelength of the incident light. On the other hand, the total scattering intensity is maximized when the Au nanorod supports a FP resonance. The wide, symmetric broadening of the scattering lobes in the x direction originates from diffraction due to the subwavelength-scale width (approximately 80 nm) of the nanorod. Note that the back focal plane of an objective lens with a high NA of 0.87, which corresponds to a polar angle of 60° , as indicated by the white dashed circle in Fig. 3(b), covers only 50% of the full hemisphere. For comparison, the differential far-field scattering cross-section distributions are calculated using FDTD simulations and plotted on the same scale as the experiment [Fig. 3(c)]. To correctly calculate the far-field distribution in an inhomogeneous

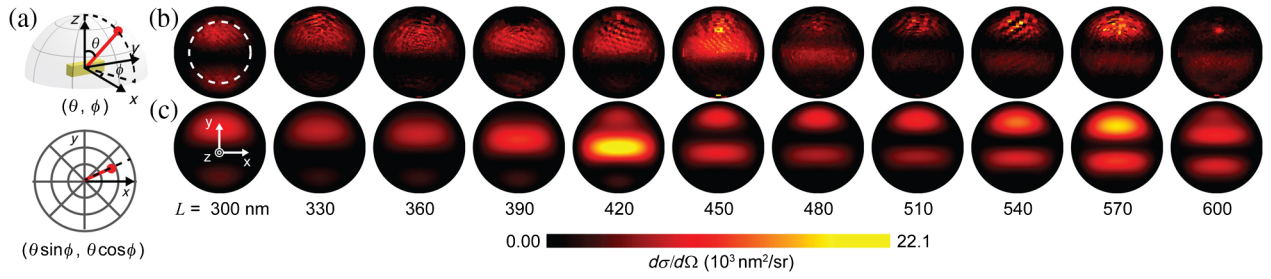


FIG. 3 (a) Far-field distribution mapping from the three-dimensional hemisphere domain onto the two-dimensional polar domain. (b) Measured far-field distribution of the differential scattering cross section of a single Au nanorod over the full hemisphere. The angular steps in the polar and azimuthal directions are 3.0° and 7.2° , respectively. The ripple interference patterns are due to scattering by tiny neighboring particles. (c) Simulated far-field distribution of the differential scattering cross section.

medium consisting of the glass substrate and air, we employ the near-to-far-field transformation based on the reciprocity theorem and transfer-matrix method [37,38].

The integration of the differential scattering cross section over the northern hemisphere enables us to quantify the total scattering cross section to air [Fig. 4(a)]. The measured integrated scattering cross section to air has a value of 4150 to 13 200 nm^2 , showing resonant behavior depending on the nanorod length. Although the simulated cross

section of 5890 to 16 800 nm^2 is approximately 1.35 times larger on average than the measured value, the FDTD simulations successfully reproduce the resonant behavior. The difference between the measured and simulated cross sections may be due mainly to imperfections in fabrication and the absorptive Cr adhesion layer [39]. The geometrical cross section of the Au nanorod, considering the cosine of the incident angle, is 8210 to 16 400 nm^2 . The plasmonic resonance allows a large scattering cross section to air that

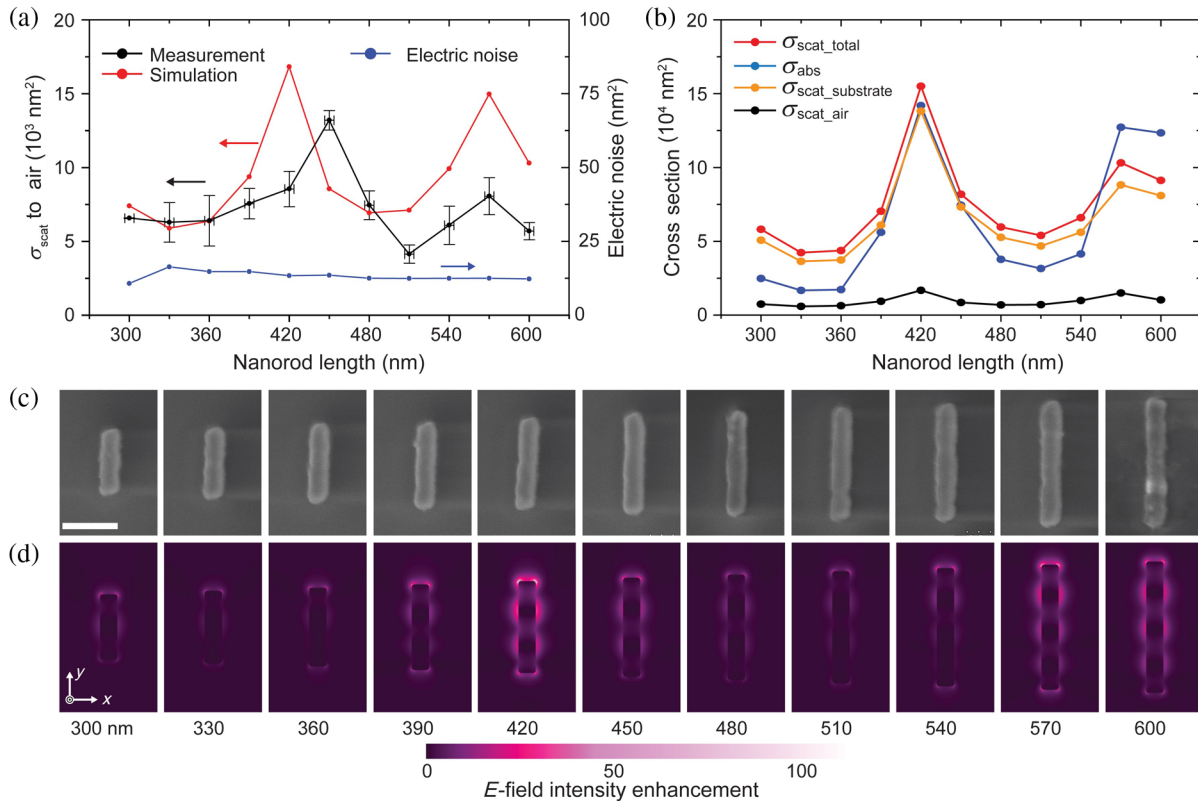


FIG. 4 (a) Measured (black) and simulated (red) integrated total scattering cross sections to the air. The horizontal error bar denotes the measurement precision of SEM. The vertical error bar corresponds to the background intensity from the neighboring area of each nanorod. The electric detection noise is also plotted (blue). (b) Simulated cross sections of the Au nanorod for total scattering (red), absorption (blue), scattering to substrate (orange), and scattering to air (black). (c) SEM images of all the fabricated Au nanorods. Scale bar, 250 nm. (d) Simulated electric field intensity enhancement profiles excited by the TIR incidence as in Fig. 2(a).

is comparable to the geometrical cross section despite the superior scattering to the high-index substrate. The scattering cross section to air is approximately 12.9%, on average, of the total scattering cross section over the full solid angle [Fig. 4(b)]. The measurement error originates mainly from the background signal by tiny neighboring particles which remain after the fabrication process and from the electric noise fluctuations of the photo-receiver during the measurement process. While the background signal varies depending on local conditions in the sample, the electric detection noise is invariant. We measure the background signal from the neighboring area of each nanorod and use the total background intensity integrated over the full hemisphere as an error bar in Fig. 4(a). The electric detection noise in the unit for the cross section is 10.7 to 16.5 nm², i.e., approximately 554 times smaller on average than the measured data, which corresponds to a signal-to-noise ratio of approximately 27.4 dB. The measurement error by the electric detection noise is only approximately 0.102% to 0.300%.

The resonant behavior of the integrated scattering cross section originates from the FP resonances of SPPs propagating along the Au nanorod. Because of its high density of optical states, the FP resonance enhances coupling between the incident light and SPPs and increases the total scattering cross section. Figures 4(c) and 4(d) show the fabricated Au nanorods and the calculated near-field distribution of the electric field intensity enhancement. The 420- and 570-nm-long nanorods in the simulations (the 450- and 570-nm-long nanorods in the experiments) support the third- and fourth-order FP resonances of SPPs, respectively. In the resonance condition of the 420-nm-long nanorod, strong intensity enhancement of approximately 110 times is achieved at the electric field maximum. The FP resonance condition depends only on the length of the Au nanorod and the propagation wave number of the SPPs. There is no relation between the FP resonance and the angular direction (θ, ϕ) to the far-field scattering radiation. Thus, even though the FP resonance contributes to the enhancement of the total or integrated scattering cross section, it does not determine the far-field distribution of the differential scattering cross section.

IV. MODEL ANALYSIS OF THE PHASE-MATCHING CONDITION

Coupling of the nanostructure-induced electromagnetic fields to the free-propagating radiation requires phase matching of the momentum (wave vector) of the light. We reveal that the phase-matching condition of the far-field scattering by the Au nanorod can be modeled as the interference of two single dipoles. Because charge-density motion of SPPs is parallel to the nanorod axis, the electric dipoles polarized along the y direction are considered in

the model analysis. The two dipoles are separated by the physical length of the nanorod L . For the far-field scattering angle θ , the optical path difference between the waves from the two emitters is $Lk_0 \sin \theta$, where k_0 is the wave vector of light in air. The phase difference between the two dipoles interfaced by the SPPs is given as $L_{\text{eff}}k_{\text{SPP}} - \pi$. Here, k_{SPP} is the propagation wave number of SPPs (calculated to be approximately 0.0188 nm⁻¹), and L_{eff} is the effective length of the nanorod including the phase pickup at both ends [32]. The additional phase of π is required because the normal vectors at the two end facets of the nanorod have opposite directions. The far-field scattering radiation is maximized by constructive interference when the total phase difference is $2m\pi$, where m is an integer. Consequently, the phase-matching condition is formulated as

$$Lk_0 \sin \theta + L_{\text{eff}}k_{\text{SPP}} = (2m + 1)\pi. \quad (1)$$

The positive sign of the second term on the left-hand side is due to asymmetric coupling of the TIR illumination to the Au nanorod. At the end of $+L/2$, direct scattering of the incident light dominates the free-propagating radiation. On the other hand, at the end of $-L/2$, scattering of the SPPs launched at the end of $+L/2$ and propagating in the $-y$ direction dominates the radiation and delivers the positive phase retardation of $+L_{\text{eff}}k_{\text{SPP}}$ [32]. Depending on the integer m , the phase-matching condition satisfying Eq. (1) has multiple solutions over the full hemisphere, producing the multilobe radiation patterns in Figs. 3(b) and 3(c).

To verify the validity of Eq. (1), we perform FDTD simulations employing two y -polarized electric dipole emitters on a glass substrate and compare the results to the other FDTD simulation and experimental measurements of the actual Au nanorods (Fig. 5). The dipole emitters are separated by L , and their phase difference is set to $L_{\text{eff}}k_{\text{SPP}} - \pi$ as in the derivation of Eq. (1). To determine the amplitude ratio of the two dipole emitters, we account for the propagation loss of SPPs, the excitation efficiency of SPPs from the TIR incident light, and the coupling efficiency of SPPs to the free-propagating radiation to air [32]. The propagation loss of the SPPs is given as $\exp(-L/L_d)$, where L_d is the propagation length, which is calculated to be approximately 1070 nm for the 80-nm-wide and 50-nm-thick nanorod. As shown in Figs. 5(a) and 5(b), the scattering radiation of the Au nanorod is well reproduced by the interference between the radiations from the two dipole emitters.

We plot the scattering intensities obtained in the experiment [Fig. 5(c)], the FDTD simulation [Fig. 5(d)], and the dipole radiation interference simulation [Fig. 5(e)] along the meridian parallel to the nanorod axis as a function of the polar angle and nanorod length. The curves of the phase-matching solutions for $m = 1$ and $m = 2$ are also overlaid on the plots (white solid lines). The measured scattering

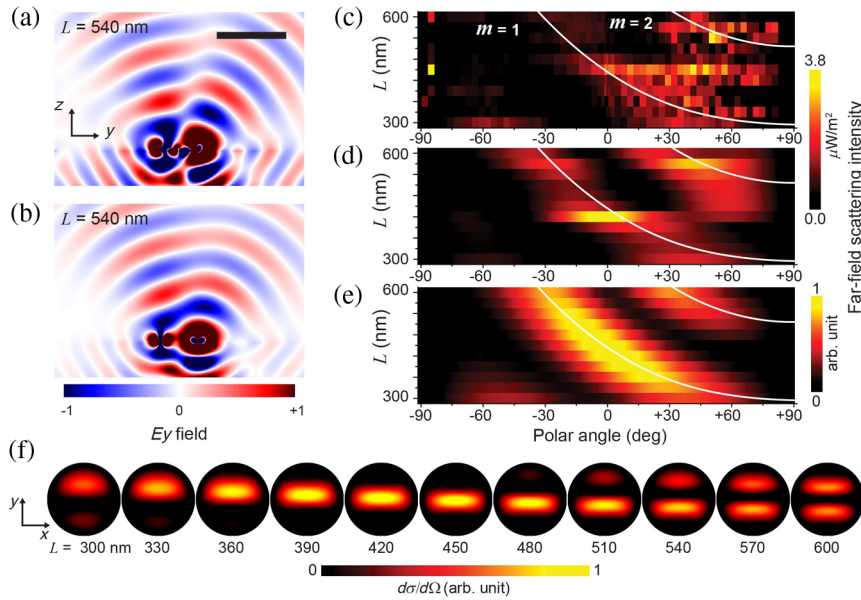


FIG. 5 Model analysis of the phase-matching condition. Snapshots of the E_y -field profile of (a) the light scattered by the Au nanorod and (b) the radiation of two dipole emitters. Scale bar, $1 \mu\text{m}$. (c)–(e) Plot of the scattering intensity along the meridian parallel to the nanorod axis as a function of the polar angle and nanorod length. The plots are obtained from (c) the experiment, (d) the FDTD simulation of the Au nanorod, and (e) the dipole radiation interference simulation, respectively. (f) Simulated far-field radiation distribution of two dipole emitters over the full hemisphere to air.

intensity is distributed with good agreement along the phase-matching solution curves [Fig. 5(c)]. The tail of the scattering lobe related to the phase-matching solution for $m = 0$ is also observed around $L = 300 \text{ nm}$ and $\theta = -60^\circ$. Although the scattering intensity becomes weaker as the polar angle approaches the horizon ($\theta = \pm 90^\circ$), phase-matching solutions exist for all polar angles θ . The FDTD simulation of the actual Au nanorod [Fig. 5(d)] agrees well with the measurements and supports the validity of the phase-matching model given by Eq. (1). As shown in Fig. 5(f), the FDTD simulation of the dipole radiation interference successfully reproduces the features of the measured and simulated far-field scattering distributions of the actual Au nanorod in Figs. 3(b) and 3(c), including the position and shape of the scattering radiation lobes. The diffraction over the meridian perpendicular to the nanorod axis (parallel to the y axis) due to the subwavelength-scale width (approximately 80 nm) of the nanorod is also excellently reproduced. Only the changes in the total scattering intensity influenced by the FP resonances of the SPPs cannot be modeled. We also note that the multipole expansion can provide a phenomenological fitting to the far-field scattering distribution [40], but it requires several higher-order terms to describe the underlying behavior of the SPPs [32].

V. CONCLUSIONS

In summary, we present a quantitative, isolated measurement of far-field scattering by a single nanostructure on the wavelength scale by combining direct solid-angle scanning and TIR illumination. Both the integrated and differential far-field scattering cross sections of a single Au nanorod over the full hemisphere are measured. We experimentally reveal that the far-field distribution of the differential scattering cross section is determined by the

phase-matching condition, whereas the total scattering cross section depends entirely on the plasmonic FP resonances. The dipole radiation interference model provides simple but precise analysis of the plasmonic scattering properties of the Au nanorod. We believe that the quantitative and angle-resolved far-field scattering measurement can provide the fundamental information required to evaluate the performance of nano-optical elements and materials. Furthermore, our far-field distribution scanner can be combined with a spectroscopy system to enable the investigation of nano-optical phenomena in energy- (wavelength) momentum (wave vector) space.

ACKNOWLEDGMENTS

M.-K. S. acknowledges support for this work by National Research Foundation of Korea (Grants No. 2017R1A2B2009117, No. 2017R1A4A1015426, No. 2016R1D1A1B03935938, No. 2014M3C1A3052537, and No. 2014M3A6B3063709). H.-G. P. acknowledges support for this work by the National Research Foundation of Korea (Grant No. 2009-0081565).

- [1] L. Novotny and N. van Hulst, Antennas for light, *Nat. Photonics* **5**, 83 (2011).
- [2] R. Adato and H. Altug, *In-situ* ultra-sensitive infrared absorption spectroscopy of biomolecule interactions in real time with plasmonic nanoantennas, *Nat. Commun.* **4**, 2154 (2013).
- [3] M. W. Knight, H. Sobhani, P. Nordlander, and N. J. Halas, Photodetection with active optical antennas, *Science* **332**, 702 (2011).
- [4] N. Fang, H. Lee, C. Sun, and X. Zhang, Sub-diffraction-limited optical imaging with a silver superlens, *Science* **308**, 534 (2005).

- [5] A. Pors and S. I. Bozhevolnyi, Plasmonic metasurfaces for efficient phase control in reflection, *Opt. Express* **21**, 27438 (2013).
- [6] L. Verslegers, P. B. Catrysse, Z. Yu, J. S. White, E. S. Barnard, M. L. Brongersma, and S. Fan, Planar lenses based on nanoscale slit arrays in a metallic film, *Nano Lett.* **9**, 235 (2009).
- [7] L. Huang, X. Chen, H. Mühlenbernd, H. Zhang, S. Chen, B. Bai, Q. Tan, G. Jin, K.-W. Cheah, C.-W. Qiu, J. Li, T. Zentgraf, and S. Zhang, Three-dimensional optical holography using a plasmonic metasurface, *Nat. Commun.* **4**, 2808 (2013).
- [8] K. Chen, A. R. B. de Castro, and Y. R. Shen, Surface-Enhanced Second-Harmonic Generation, *Phys. Rev. Lett.* **46**, 145 (1981).
- [9] M. Lippitz, M. A. van Dijk, and M. Orrit, Third-harmonic generation from single gold nanoparticles, *Nano Lett.* **5**, 799 (2005).
- [10] W. Cai, A. P. Vasudev, and M. L. Brongersma, Electrically controlled nonlinear generation of light with plasmonics, *Science* **333**, 1720 (2011).
- [11] P. Ginzburg, A. Krasavin, Y. Sonnefraud, A. Murphy, R. J. Pollard, S. A. Maier, and A. V. Zayats, Nonlinearly coupled localized plasmon resonances: Resonant second-harmonic generation, *Phys. Rev. B* **86**, 085422 (2012).
- [12] H. Li, J. W. Noh, Y. Chen, and M. Li, Enhanced optical forces in integrated hybrid plasmonic waveguides, *Opt. Express* **21**, 11839 (2013).
- [13] R. Thijssen, E. Verhagen, T. J. Kippenberg, and A. Polman, Plasmon nanomechanical coupling for nanoscale transduction, *Nano Lett.* **13**, 3293 (2013).
- [14] H. C. van de Hulst, *Light Scattering by Small Particles* (Dover Publications, New York, 1957).
- [15] A. Alu and N. Engheta, Tuning the scattering response of optical nanoantennas with nanocircuit loads, *Nat. Photonics* **2**, 307 (2008).
- [16] Y. H. Fu, A. I. Kuznetsov, A. E. Miroshnichenko, Y. F. Yu, and B. Luk'yanchuk, Directional visible light scattering by silicon nanoparticles, *Nat. Commun.* **4**, 1527 (2013).
- [17] S. Person, M. Jain, Z. Lapin, J. J. Sáenz, G. Wicks, and L. Novotny, Demonstration of zero optical backscattering from single nanoparticles, *Nano Lett.* **13**, 1806 (2013).
- [18] M. Husnik, M. W. Klein, N. Feth, M. König, J. Niegemann, K. Busch, S. Linden, and M. Wegener, Absolute extinction cross-section of individual magnetic split-ring resonators, *Nat. Photonics* **2**, 614 (2008).
- [19] S. A. Mann, B. Sciacca, Y. Zhang, J. Wang, E. Kontoleta, H. Liu, and E. C. Garnett, Integrating sphere microscopy for direct absorption measurements of single nanostructures, *ACS Nano* **11**, 1412 (2017).
- [20] M. Husnik, S. Linden, R. Diehl, J. Niegemann, K. Busch, and M. Wegener, Quantitative Experimental Determination of Scattering and Absorption Cross-Section Spectra of Individual Optical Metallic Nanoantennas, *Phys. Rev. Lett.* **109**, 233902 (2012).
- [21] C. Langhammer, B. Kasemo, and I. Zorić, Absorption and scattering of light by Pt, Pd, Ag, and Au nanodisks: Absolute cross sections and branching ratios, *J. Chem. Phys.* **126**, 194702 (2007).
- [22] A. G. Curto, T. H. Taminiâu, G. Volpe, M. P. Kreuzer, R. Quidant, and N. F. van Hulst, Multipolar radiation of quantum emitters with nanowire optical antennas, *Nat. Commun.* **4**, 1750 (2013).
- [23] S. Ivana, T. Christelle, and A. F. Koenderink, Fourier microscopy of single plasmonic scatterers, *New J. Phys.* **13**, 083019 (2011).
- [24] T. H. Taminiâu, S. Karaveli, N. F. van Hulst, and R. Zia, Quantifying the magnetic nature of light emission, *Nat. Commun.* **3**, 979 (2012).
- [25] T. Coenen, E. J. R. Vesseur, A. Polman, and A. F. Koenderink, Directional emission from plasmonic Yagi-Uda antennas probed by angle-resolved cathodoluminescence spectroscopy, *Nano Lett.* **11**, 3779 (2011).
- [26] J. A. Kurvits, M. Jiang, and R. Zia, Comparative analysis of imaging configurations and objectives for Fourier microscopy, *J. Opt. Soc. Am. A* **32**, 2082 (2015).
- [27] J. M. Geffrin, B. García-Cámara, R. Gómez-Medina, P. Albella, L. S. Froufe-Pérez, C. Eyraud, A. Litman, R. Vaillon, F. González, M. Nieto-Vesperinas, J. J. Sáenz, and F. Moreno, Magnetic and electric coherence in forward-and back-scattered electromagnetic waves by a single dielectric sub-wavelength sphere, *Nat. Commun.* **3**, 1171 (2012).
- [28] J. Motohisa, Y. Kohashi, and S. Maeda, Far-field emission patterns of nanowire light-emitting diodes, *Nano Lett.* **14**, 3653 (2014).
- [29] G. Gay, O. Alloschery, B. Viaris de Lesegno, C. O'Dwyer, J. Weiner, and H. J. Lezec, The response of nanostructured surfaces in the near field, *Nat. Phys.* **2**, 262 (2006).
- [30] J.-H. Kang, S.-K. Kim, K.-Y. Jeong, Y.-H. Lee, M.-K. Seo, and H.-G. Park, Polarization-resolved far-field measurement of single-cell photonic crystal lasing modes, *Appl. Phys. Lett.* **98**, 211116 (2011).
- [31] J. R. Krenn, G. Schider, W. Rechberger, B. Lamprecht, A. Leitner, F. R. Aussenegg, and J. C. Weeber, Design of multipolar plasmon excitations in silver nanoparticles, *Appl. Phys. Lett.* **77**, 3379 (2000).
- [32] See Supplemental Material at <http://link.aps.org/supplemental/10.1103/PhysRevApplied.8.054024> for more technical details.
- [33] L. Novotny, Effective Wavelength Scaling for Optical Antennas, *Phys. Rev. Lett.* **98**, 266802 (2007).
- [34] T. H. Taminiâu, F. D. Stefani, and N. F. van Hulst, Optical nanorod antennas modeled as cavities for dipolar emitters: Evolution of sub- and super-radiant modes, *Nano Lett.* **11**, 1020 (2011).
- [35] H. Ditlbacher, A. Hohenau, D. Wagner, U. Kreibig, M. Rogers, F. Hofer, F. R. Aussenegg, and J. R. Krenn, Silver Nanowires as Surface Plasmon Resonators, *Phys. Rev. Lett.* **95**, 257403 (2005).
- [36] D. R. Lide, *CRC Handbook of Chemistry and Physics*, 87th ed. (CRC Press/Taylor and Francis Group, Boca Raton, FL, 2006).
- [37] K. Demarest, Z. Huang, and R. Plumb, An FDTD near-to far-zone transformation for scatterers buried in stratified grounds, *IEEE Trans. Antennas Propag.* **44**, 1150 (1996).
- [38] K. C. Y. Huang, M.-K. Seo, Y. Huo, T. Sarmiento, J. S. Harris, and M. L. Brongersma, Antenna electrodes for controlling electroluminescence, *Nat. Commun.* **3**, 1005 (2012).

- [39] T. G. Habteyes, S. Dhuey, E. Wood, D. Gargas, S. Cabrini, P. J. Schuck, A. P. Alivisatos, and S. R. Leone, Metallic adhesion layer induced plasmon damping and molecular linker as a nondamping alternative, *ACS Nano* **6**, 5702 (2012).
- [40] T. Inoue and H. Hori, Theoretical treatment of electric and magnetic multipole radiation near a planar dielectric surface based on angular spectrum representation of vector field, *Opt. Rev.* **5**, 295 (1998).